

# A Permeable Triboelectric Fiber Mat with 35 V cm<sup>-2</sup> Voltage Output for Wearable Wireless Sensing Electronics

Youchao Qi, Jinxing Jiang, Fan Chen, Junhua Zhou, Jiaheng Liang, Jingjing Fu, Yongqiang Yang, Yichun Ding, Zijian Zheng, and Qiyao Huang\*

Textile-based triboelectric nanogenerators have emerged as a promising solution for self-powered wearable electronics, owing to their exceptional comfort derived from the inherent flexibility of textiles, coupled with their remarkable capability to efficiently harvest low-frequency energy from human motions. However, one primary challenge lies in how to enhance output and management efficiency without compromising comfort to meet the high-power consumption demands of electronics. Herein, a permeable triboelectric nanogenerator (pTENG) is reported with a voltage output exceeding 35 V cm<sup>-2</sup> while maintaining breathability. Such a high output of this pTENG is attributed to the enhanced dielectric constant, facilitated by the uniform distribution of liquid metal nanoparticles in the electrospun composite fiber mat. With a specially designed energy management module, the self-powering system based on pTENG can achieve 10 times faster charging speed than those regulated only by rectifiers. As a proof-of-concept demonstration, a garment integrating a pTENG, an energy management module, a temperature sensor, and a wireless transmitter is developed to form a self-powered wireless temperature sensing system, which can sense and transmit temperature data to a relay terminal module. This integration reduces reliance on external power while enabling real-time wireless health monitoring, highlighting the great potential of body area networks in personalized healthcare.

1. Introduction

Energy harvesting technology can capture ambient energies, such as mechanical, solar, and thermal energy, and convert them into electrical power. [1-5] This technology is especially appealing to wearable wireless sensing electronics used for

sports and rehabilitation exercises, where activities such as running, walking, and joint movements can be harnessed for the powering of wireless sensor electronics without the need for batteries. As a result, an uninterrupted energy supply during usage can be offered, leading to lower maintenance costs, longer device lifespan, and greater environmental friendliness compared to battery-powered systems. Commonly utilized energy harvesting technologies for extracting mechanical energy from the human body include electromagnetic induction, [6-8] piezoelectric, [9-12] and electrostatic generators.[13,14] They, however, struggle to efficiently capture the energy from the low-frequency mechanical movements of the human body (typically < 10 Hz) due to their limited conversion capabilities to lower frequency motions (generally output voltage <0.2 V).[15,16] Triboelectric nanogenerators (TENGs),[17-20] an energy-harvesting technology that is based on the coupling effects of contact electrification and electrostatic induction, has been proposed as an alternative. They exhibit an inherently high voltage output

(>10–100 V) that is independent of frequency, allowing most of the generated electrical energy to sufficiently power electronic devices operate at a threshold voltage of  $\approx 0.2-4$  V. In addition, TENGs offer advantages such as wide selection of materials, [21–24] lightweight design, [25,26] low cost, [27] and ease of scalability through advanced structural engineering. [28] Such

Y. Qi, J. Jiang, Y. Ding, Q. Huang School of Fashion and Textiles The Hong Kong Polytechnic University Hong Kong SAR 999077, P. R. China E-mail: qi-yao.huang@polyu.edu.hk

The ORCID identification number(s) for the author(s) of this article can be found under https://doi.org/10.1002/smll.202504556

© 2025 The Author(s). Small published by Wiley-VCH GmbH. This is an open access article under the terms of the Creative Commons Attribution License, which permits use, distribution and reproduction in any medium, provided the original work is properly cited.

DOI: 10.1002/smll.202504556

F. Chen, J. Zhou, J. Liang, J. Fu, Y. Yang, Z. Zheng
Department of Applied Biology and Chemical Technology
Faculty of Science
The Hong Kong Polytechnic University
Hong Kong SAR 999077, P. R. China
Z. Zheng, Q. Huang
Research Institute for Intelligent Wearable Systems
The Hong Kong Polytechnic University
Hong Kong SAR 999077, P. R. China
Z. Zheng
Research Institute for Smart Energy
The Hong Kong Polytechnic University
Hong Kong SAR 999077, P. R. China
Z. Zheng
PolyU-Wenzhou Technology and Innovation Research Institute
Wenzhou, Zhejiang 325024, P. R. China



\_ SMQ

www.small-journal.com

characteristics enable the TENGs to be more adaptable at harvesting micromechanical energy generated by human motion compared to counterparts.

To date, TENGs have attracted widespread research interest for powering smart wireless sensing electronics.<sup>[29–32]</sup> The stateof-the-art TENGs can achieve high voltage output typically exceeding 30 V cm<sup>-2</sup>, which can meet the energy requirement of most wearable wireless sensing electronics. TENGs with high voltage output are primarily developed by using highly electronegative thin-film materials (such as polytetrafluoroethylene, fluorinated ethylene propylene, etc.).[33] However, the lack of permeability to air and moisture in these thin-film materials poses a barrier to practical applications in prolonged use, potentially leading to wearing discomfort over extended periods.[34] Developing TENGs on the basis of textile materials and structures shows promise in addressing the lack of permeability in thin-film devices, which is attributed to the fibrous configuration of textiles that can impart intrinsic breathability to TENG textiles.<sup>[35]</sup> As such, textile-based TENGs can not only offer excellent softness, air and moisture permeability that leads to wearing comfort characteristic, but also the ability to generate electricity from the body movement to power wearable sensors. Nevertheless, textile-based TENGs encounter hurdles in meeting the power demands of wireless sensing electronics that typically possess high power consumption requirements ( $\mu W \sim mW$ ).<sup>[36]</sup> This is due to the relatively low output voltage (typically <30 V cm<sup>-2</sup>) of textile-based TENGs compared to those of the thin-film TENGs, and the inherent limitation of pulsed alternating voltage in powering electronics that require a stable direct voltage of 2.5-4 V. Although energy management technology, such as rectification and buck-boost conversion, has been developed to transform the pulsed alternating current output of TENGs into a stable direct current output for reliably powering the sensors,[37,38] challenging still persist in boosting the output of TENG textiles and maximizing the efficient utilization of the generated energy.

To address the above-mentioned challenge, we herein report a permeable triboelectric nanogenerator (pTENG) with a high output voltage of over 35 V cm<sup>-2</sup>. pTENG is composed of a high-performance triboelectric composite fiber mat (denoted as LMPT), which is developed by the electrospinning of liquidmetal (LM)-embedded PVDF-TrFE (Poly(vinylidene fluoride-cotrifluoroethylene)). The fibrous structure of the electrospun LMPT composite fiber mat facilitates rapid pathways for the permeation of air and moisture, thereby endowing the pTENG with high air permeability (up to 8.8 mm s<sup>-1</sup>) and moisture permeability (up to 630 g m<sup>-2</sup> day<sup>-1</sup>). Importantly, the incorporation of LM nanoparticles in LMPT significantly boosts the output performance of the as-formed pTENG, due to the increased dielectric constant of the LMPT. pTENG consisting of LMPT possesses a exceptionally high voltage output exceeding 35 V cm<sup>-2</sup> and a high charge density of 3.36 nC cm<sup>-2</sup>, surpassing those of its counterpart (pTENG made of PVDF-TrFE fiber mat without embedding LM nanoparticle) by 83% and 46%, respectively. To maximize the utilization of the generated electricity from pTENG, an energy management module incorporating buck-boost current regulation, active voltage monitoring, and stabilized output control is further designed. By integrating this energy management module, LMPT-based pTENG can charge a commercial 0.68 mF capacitor to 3.1 V in 300 s, showcasing a remarkable ten-fold enhancement in charging speed compared to the counterpart. As a proof-of-concept demonstration, pTENGs are utilized to rapidly power a wireless sensing system with power consumption of  $\approx$ 22.5 mW, facilitating the sensing and real-time transmission of temperature data to the cloud through Wireless Fidelity (Wi-Fi). This reported work demonstrates the successful integration of human motion energy harvesting, efficient energy management, and wireless sensing technologies. Such an integration enables the real-time healthcare monitoring while maintaining the wearability of wearable technologies, presenting substantial application potential in areas such as wireless sensing electronics and body area network.

#### 2. Results and Discussion

#### 2.1. Fabrication and Characterization of LMPT

The key component for constructing the pTENG is LMPT, which is an electrospun triboelectric fiber mat of PVDF-TrFE embedded with LM nanoparticles (Figure 1a). The fabrication process of the LMPT is described in detail in the Experimental Section. Briefly, the electrospinning dope for LMPT is prepared by mixing a PVDF-TrFE solution with a stable suspension of LM nanoparticles (Eutectic Gallium (Ga)-Indium (In) Alloy) at different ratios (Figure S1, Supporting Information). The LM nanoparticle suspension used herein is prepared by ultrasonication, through which the LM is converted into nanosized spheres with diameters approximately ranging from 40 to 450 nm (Figure S2, Supporting Information). LMPT is then fabricated by electrospinning the LM-mixed PVDF-TrFE dope onto a piece of nickel (Ni)-coated fabric (denoted as Ni fabric), resulting in the formation of a single triboelectric electrode. By pairing with another piece of Ni fabric as the opposing triboelectric electrode, an all-textile-based pTENG is constructed, which can serve as a power source unit for driving wearable wireless electronics.

The introduction of LM significantly influences the morphological and mechanical properties of LMPT. With the inclusion of LM nanoparticles, LMPT exhibits a grey color distinct from the electrospun PVDF-TrFE (denoted as PVDF) fiber mat without LM loading (Figure 1b; Figure S3, Supporting Information). Scanning electron microscope (SEM) images of LMPT reveal that electrospun fibers, approximately ranging in diameter from 300 nm to 1.3 µm, are randomly arranged within the matrix, with an even distribution of LM beads partially embedded into the fibers (Figure 1c,d). The distribution of LM in the PVDF fibrous matrix is further investigated by Transmission Electron Microscopy (TEM). In addition to being partially embedded into the PVDF fiber due to their oversize compared to the fiber (Figure 1d), LM nanoparticles with dimensions smaller than 300 nm are fully incorporated within the fiber (Figure 1e). It is also noticed that there are large spindles, typically ranging from 2.5 to 5 µm in dimensions, presented in LMPT, which may be attributed to the aggregation of LM nanoparticles combined with the polymeric matrix (Figure S4, Supporting Information). Such a phenomenon becomes more pronounced as the LM content increases from 0.25% to 5% (by weight ratio to the electrospinning dope) (Figure S5, Supporting Information). As a result of these morphological changes, the tensile properties of LMPTs exhibit

16136829, 2025, 34, Downloaded from https://onlinelibrary.wiley.com/doi/10.1002/smll.202504556 by HONG KONG POLYTECHNIC UNIVERSITY HU NG HOM, Wiley Online Library on [02/10/2025]. See the Terms

(https://onlinelibrary.wiley.com/terms-and-conditions) on Wiley Online Library for rules of use; OA articles are governed by the applicable Creative Commons License

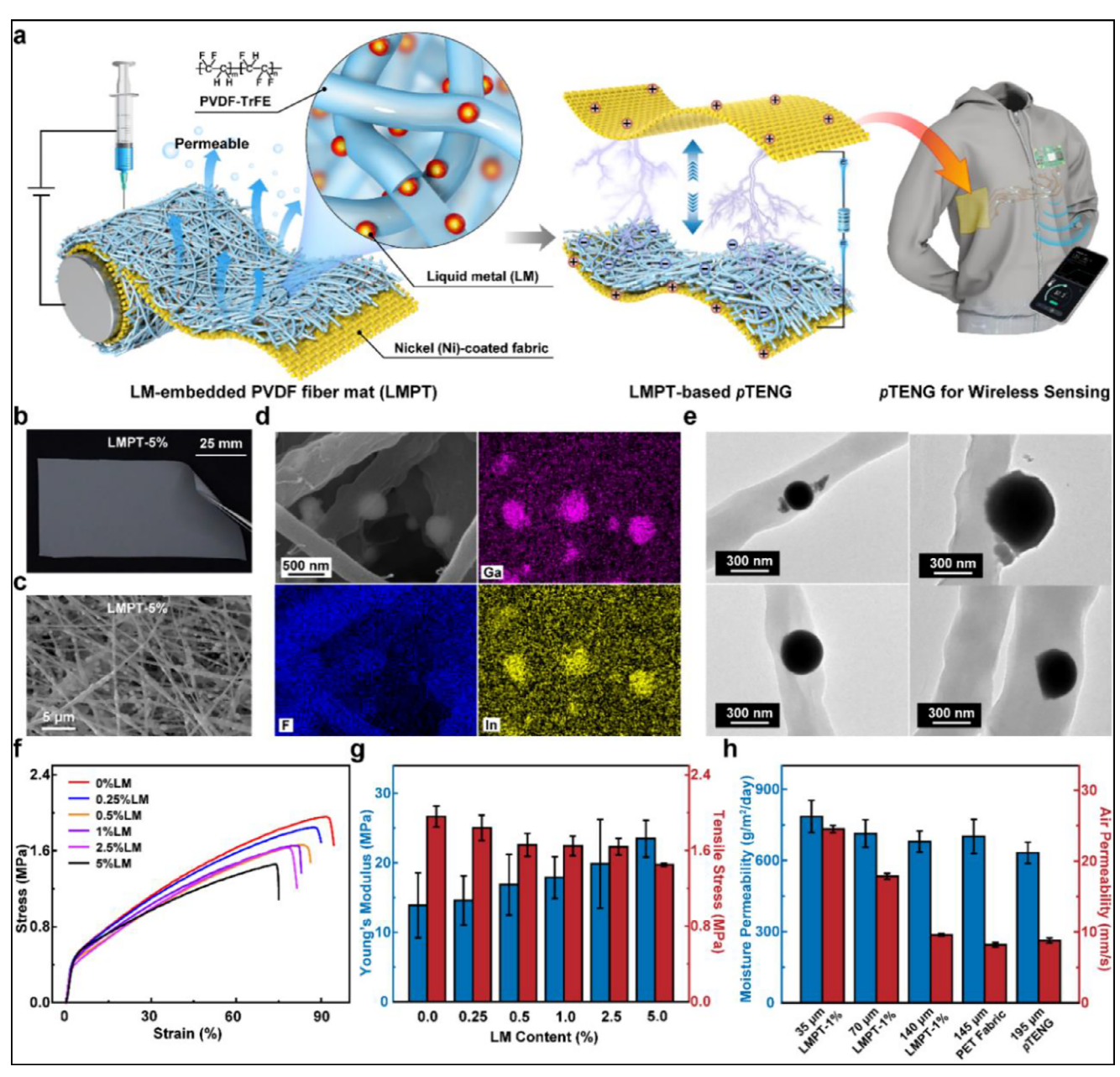


**Figure 1.** Fabrication and characterization of Liquid-metal (LM)-embedded PVDF-TrFE triboelectric composite fiber mat (denoted as LMPT) for permeable triboelectric nanogenerator (pTENG). a) Design of LMPT and its pTENG for application in powering wireless sensing. b) Digital image and c) Scanning electron microscopy (SEM) image of LMPT-5% (5% is the weight ratio of liquid metal to the electrospinning dope). d) SEM elemental mapping of LMPT-1% showing the distribution of LM particles in the fiber mat (1% is the weight ratio of liquid metal to the electrospinning dope). e) Transmission electron microscopy (TEM) image showing the distribution of LM nanoparticles within the PVDF-TrFE fibers. f) Stress-strain curves for the LMPT with varying LM contents. g) Young's modulus and tensile strength of LMPT with varying LM contents (the data were from the mean of five sets of experimental data, and the error bar was taken from the standard deviation). h) Moisture and air permeability of LMPT-1% with varying thicknesses, pTENG, and PET fabric (the data were from the mean of five sets of experimental data, and the error bar was taken from the standard deviation).

corresponding variations. In comparison to the PVDF fiber mat without LM loading, all the LMPT specimens display a decrease in the tensile breaking strength. The Young's modulus of LMPT shows an opposite trend to its tensile strength, exhibiting enhanced deformation resistance with increasing LM content (Figure 1f.g). While the breaking strain of the PVDF fiber mat

can reach up to 92% at a breaking stress of 1.96 MPa, the breaking strain of LMPT with only 0.25% LM loading decreased to 88% with a breaking stress of 1.84 MPa. With a higher LM loading content of 5%, LMPT achieves a strain of only  $\approx\!75\%$  under a breaking stress of 1.5 MPa (Figure 1f). The increased LM nanoparticles within the composite fiber mat may lead to the disruption

16136829, 2025, 34, Downloaded from https://onlinelibrary.wiley.com/doi/10.1002/smll.202504556 by HONG KONG POLYTECHNIC UNIVERSITY HU NG HOM, Wiley Online Library on [0210.2025]. See the Terms and Conditions

thtps://onlinelibrary.wiley.com/terms-and-conditions) on Wiley Online Library for rules of use; OA articles are governed by the applicable Creative Commons License

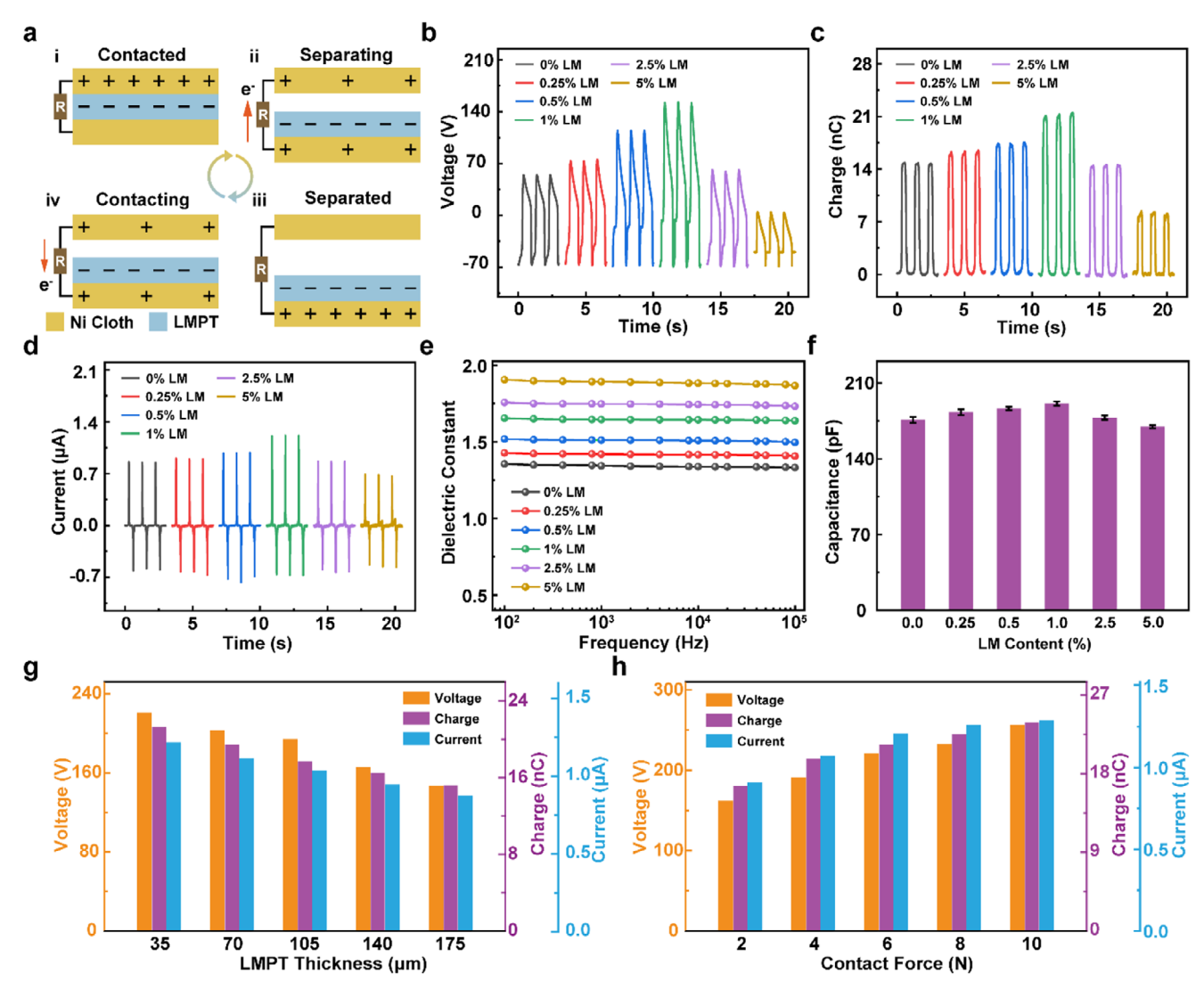


Figure 2. Enhanced electric output of pTENG enabled by LMPT. a) Mechanism of electricity generation in pTENG. b) Open-circuit voltage, c) Transferred charge, and d) Short-circuit current of the pTENG assembled with LMPTs of different LM contents. e) Dielectric constant of LMPT with different LM contents. f) Capacitance of the pTENG assembled with LMPTs of different LM contents (the data were from the mean of five sets of experimental data, and the error bar was taken from the standard deviation). g,h) Open-circuit voltage, transferred charge, and short-circuit current of the pTENG at varying LMPT thicknesses and different contact forces.

of the polymeric structure, resulting in the decline in mechanical performance. [39,40] Nevertheless, the mechanical strength and softness of LMPT well align with those of textile materials and human skin, [41] thereby rendering LMPT suitable for applications in wearables and smart textiles. Additionally, the porous nature of the fibrous composite matrix allows LMPTs of various thickness to exhibit excellent air (up to 24 mm s<sup>-1</sup>) and moisture permeability (up to 780 g m<sup>-2</sup> day<sup>-1</sup>) (Figure 1h). When pairing the 35 µm-LMPT with Ni-fabrics for the assembly of pTENG, such pTENG, with a total thickness of 195 µm, still exhibits promising air (8.8 mm  $s^{-1}$ ) and moisture permeability (630 g m<sup>-2</sup> day<sup>-1</sup>). These characteristics, akin to those of conventional textile fabrics, are particularly advantageous for pTENGs in applications involving extended collection of kinetic energy over the long term.

#### 2.2. Enhanced Electric Output of pTENG Enabled by LMPT

pTENG, consisting of one layer of LMPT spun on Ni fabric as the bottom electrode (negative triboelectric layer) and one layer of Ni fabric as the top electrode (positive triboelectric layer), is assembled for electric output testing. When the two electrodes come into contact, negative charges generated in the bottom electrode transfer from the Ni fabric to the surface of the LMPT, resulting in an equal amount of net charge appearing on the surfaces of the Ni fabric and LMPT, respectively (Figure 2a-i). When the two pieces of textile start to separate from each other, electrons flow through the external load from the bottom electrode to the top electrode to balance the charges (Figure 2a-ii). Once the two pieces of textile are fully separated, all electrons are transferred to the top electrode (Figure 2a-iii). As the two electrodes begin to come into





www.small-journal.com

contact again, the electrons on the top electrode flow back to the bottom electrode until full contact is achieved (Figure 2a-iv). This continuous contact-separation cycle between the two electrodes generates alternating electrical output. Figure 2b-d exhibits the electric output performance of pTENG fabricated with LMPTs of different LM contents. With an increase in LM content to 1%, pTENG achieve the voltage, charge, and current output of up to 220 V ( $\approx$ 35 V cm<sup>-2</sup>), 21 nC, and 1.2  $\mu$ A, respectively, showcasing the performance enhancements of ≈83%, 46%, and 42% compared to the pTENG made with pristine PVDF fiber mat without loading LM. To the best of our knowledge, this LMPT-based pTENG represents the highest normalized electric output among the literature of textile-based TENGs (Table S1, Supporting Information).[42-57] However, further increasing the LM content in the fiber mat composite does not lead to the significant improvement in the electric output of pTENG. Instead, the output performance of the LMPT-based pTENG with a 5% loading of LM is even lower than that of the pTENG made with pristine PVDF fiber mat.

The enhancement of pTENG performance with the increasing loading of LM up to 1% may be attributed to the incorporation of the conductive LM nanoparticles into PVDF fibrous matrix, leading to the trapping of triboelectric charges<sup>[42]</sup> and the increased dielectric constant. During the preparation of LM nanoparticles for electrospinning dope via ultrasonication, the surface of LM rapidly oxidizes to form a Ga<sub>2</sub>O<sub>3</sub> layer. [58] This Ga<sub>2</sub>O<sub>3</sub> layer, a semiconductor with abundant interface states, plays a crucial role in the transfer process of the triboelectric charges.<sup>[42]</sup> During the contact-separation cycles of the two triboelectric layers in the pTENG (Figure 2a), the accumulation of opposite triboelectric charges leads to the changes in the interface states of Ga<sub>2</sub>O<sub>3</sub> (Figure S6, Supporting Information). When the LMPT layer is uncharged, Ga2O3 remains in a flat-band state, with no electron capture occurring (Figure S6a, Supporting Information). As negative charges accumulate on the LMPT surface, a potential difference arises due to the charge imbalance between the PVDF-TrFE layer on the LMPT surface and the underlying PVDF-TrFE fibers. This potential difference drives electrons from the external circuit into the Ni electrode and subsequently into the PVDF-TrFE fibers, where these electrons are captured by the interface states of Ga<sub>2</sub>O<sub>3</sub>, facilitating rapid charge transfer (Figure S6b, Supporting Information). As LM content increases, the density of interface states rises, promoting more efficient charge transfer and thereby enhancing pTENG performance.

More importantly, such an integration of PVDF-TrFE with LM nanoparticles also enables an increase in dielectric constant of the composite fiber mat, which can benefit the capacitance of the triboelectric electrode and thereby lead to the enhancement in the electric output of the as-assembled *p*TENG.<sup>[59]</sup> We investigate the impact of LM incorporation on the dielectric constant of LMPT (Figure 2e). The dielectric constant of LMPT exhibited a significantly enhancement, increased from 1.34 to 1.89 at the frequency of 1000 Hz with the content of LM increasing from 0% to 5%. Especially, the dielectric constant of LMPT embedded with 1% LM exhibits a 23% increase in comparison with that of the pristine PVDF fiber mat. Such an enhancement in dielectric constant can be attributed to the sufficient composite dielectric network formed by the incorporated LM nanoparticles (Figure 1c–e), which can significantly improve the overall

dielectric performance of the material. [40] Further increasing the dielectric constant, in principle, can be achieved by increasing the LM content in the electrospinning dope. However, when the LM content exceeds 1% in LMPT composite, a significant alteration in the fibrous morphology occurs as illustrated in Figures S4 and S5, Supporting Information, where spindles of the aggregation of LM with polymeric matrix are formed. Such morphological changes may lead to the development of local conductive networks, resulting in charge leakage during the contactseparation of the TENG devices. Consequently, the electrical output of the pTENG diminishes, which is reflected in the results of electrical output (Figure 2b-d). The impact of higher LM loading (i.e., larger than 1%) in LMPT on the performance degradation of pTENG can also be verified by the capacitance changes of the pTENG. The capacitance of the pTENG increases from 175 to 190 pF and then decreases to 170 pF as the LM content rises from 0% to 5%. With 1% LM, the capacitance is  $\approx$ 8% higher than that of pristine PVDF fiber mat, while at 5% LM, it decreases by  $\approx$ 2.8% (Figure 2f). This capacitance change is mainly attributed to the increased spindles that may reduce the effective contact area (Note \$1, Supporting Information) between the triboelectric electrodes, degrading the output performance of the pTENG. We further investigate the variation of surface potential of LMPT with respect to LM concentration (Figure S7, Supporting Information). The results show that the surface potential of the LMPT increases with LM content up to 1%, indicating that a higher concentration of LM facilitates more effective storage and retention of triboelectric charges on the surface. Such enhanced surface charge retention is expected to improve electrostatic induction and, consequently, the overall output performance of the pTENG. However, when the LM content exceeds 1%, the surface potential decreases, which is consistent with the observed trends in output performance and capacitance. This decline is likely due to the formation of local conductive pathways and increased surface charge leakage caused by LM aggregation, which impedes effective charge accumulation on the surface. These findings further confirm the importance of optimizing LM concentration to modulate the surface electrostatic environment and maximize the triboelectric performance of the pTENG.

Upon mechanism analysis, LMPT with 1% LM loading, which provides the optimized output performance, is chosen for the further performance characterization of pTENG. The impacts of fiber mat thickness and applied external forces on the electrical performance of the pTENG are evaluated. A thinner triboelectric layer can result in a higher electrical performance of the pTENG (Figure 2g, Figure S8a-c, Supporting Information). When the LMPT thickness decreases from 175 to 35 µm, the voltage, charge, and current outputs of the pTENG increase by  $\approx 52\%$ , 40%, and 39%, respectively. A thinner dielectric layer is beneficial for increasing the capacitance of the pTENG. It can be modeled as a series-connected capacitive pulsed voltage source, [59] expressed as  $1/C_{pTENG} = 1/C_{LMPT} + 1/C_{spacer}$ , where  $C_{pTENG}$  is the total capacitance of the pTENG,  $C_{LMPT}$  is the capacitance of LMPT, and  $C_{\mbox{\tiny spacer}}$  is the capacitance between the positive and negative triboelectric electrodes. As the thickness of LMPT decreases, C<sub>IMPT</sub> increases, leading to a higher total capacitance and charge storage of the pTENG, thereby enhancing its output performance. Nevertheless, excessively thin layers are prone to damage under external force due to increased friction, compromising the

16136829, 2025, 34, Downloaded from https://olinelibrary.wiley.com/doi/10.1002/sml. 202504556 by HONG KONG PCLYTECHNIC UN VERSITY HU NG HOM, Wiley Online Library on [02/10/2025]. See the Terms and Conditions (https://olinelibrary.wiley.com/terms-ad-conditions) on Wiley Online Library for rules of use; O.A articles are governed by the applicable Ceataive Commons Licenses

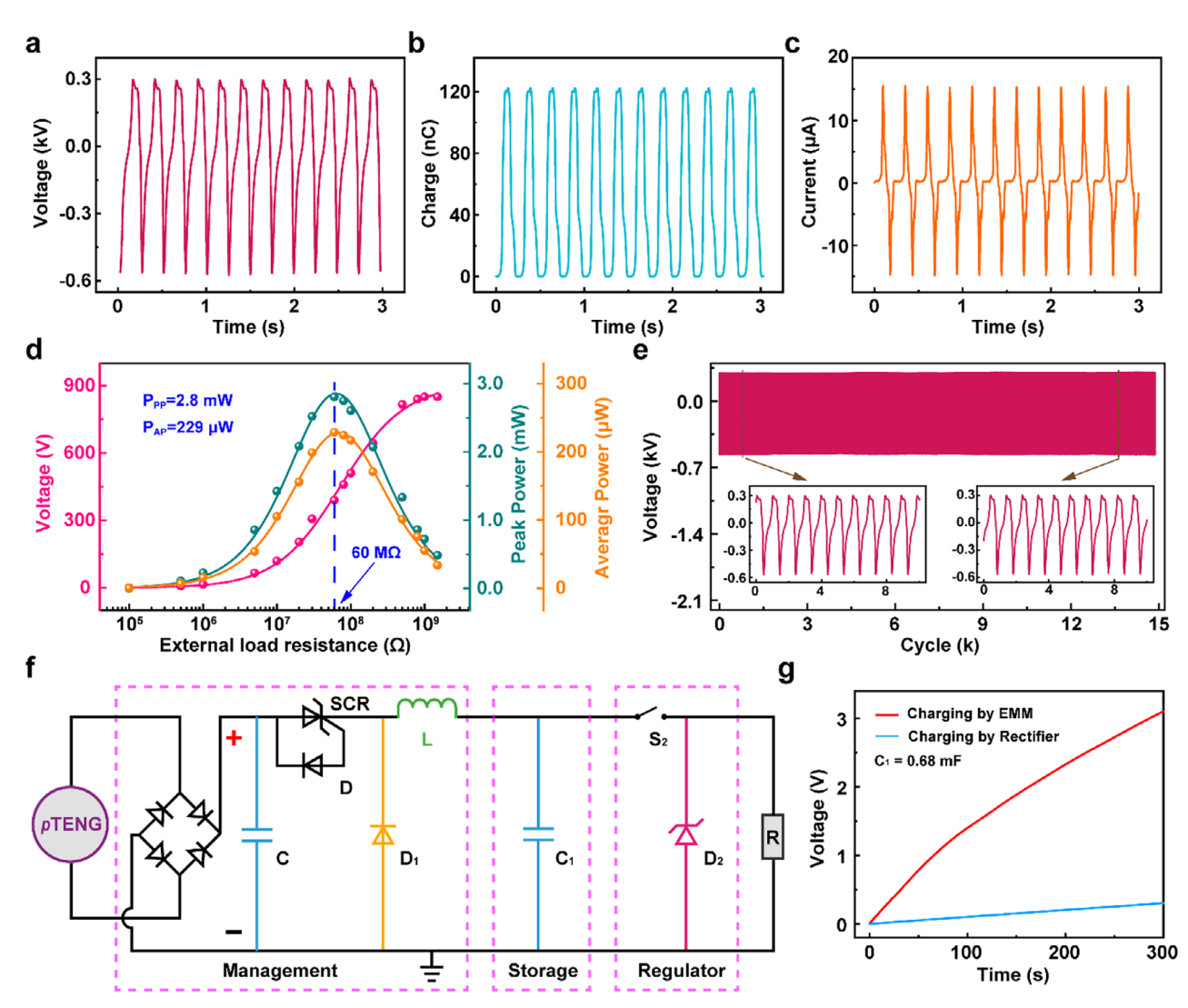


**Figure 3.** Output performance and efficient energy management of the pTENG. a) Open-circuit voltage, b) Transferred charge, c) Short-circuit current, and d) Power characteristics of pTENG at a working frequency of 4 Hz. e) Voltage output stability of pTENG over 15000 cycles. f) Design of energy management module (EMM) for pTENG. g) Comparison of the efficiency of charging a capacitor through EMM and a rectifier.

device's durability. Therefore, for wearable pTENG fabrication using LMPT, we select a 1% LM-doped LMPT layer with a thickness of 35 µm as the triboelectric layer to balance performance and stability. Higher electrical output can be achieved upon the application of greater external force to the pTENG (Figure 2h, Figure S8d-f, Supporting Information). Increasing the applied external force from 2 to 10 N can lead to the increase in the voltage, charge, and current output of pTENG by ≈58%, 44%, and 42%, respectively. Such an enhancement is attributed to the increased external force that effectively enlarges the effective contact area between the two triboelectric electrodes. Furthermore, the pTENG also exhibits promising electrical output performance under high-humidity conditions. Even at a relative humidity of 85%, the open-circuit voltage, transferred charge, and short-circuit current still retain 75%, 78%, and 71%, of their valued measured under ambient conditions, respectively (Figure S9, Supporting Information). This moderate decline is mainly due to the adsorbed water molecules on the dielectric surface that result in charge leakage and suppression of charge accumulation. The washing durability of the pTENG is also evaluated by following the Standard AATCC 135. The device retains stable performance after 10 washing cycles (Figure S10, Supporting Information). The output voltage, transferred charge, and short-circuit current exhibited only minor decreases of  $\approx$ 15%, 13%, and 12%, respectively.

## 2.3. Energy Management for pTENG

The incorporation of LM nanoparticles into the *p*TENG has led to remarkable improvements in its performance, providing new insights into material optimization for energy harvesting. In particular, with an LMPT area of 25 cm², *p*TENG demonstrates enhanced output characteristics, achieving maximum output voltage of 825 V, charge of 120 nC, and current of 15 µA (**Figure 3a–c**). More importantly, *p*TENG based on LMPT can achieve a peak

16136829, 2025, 34, Downloaded from https://onlinelibrary.wiley.com/doi/10.1002/smll.202504556 by HONG KONG POLYTECHNIC UNIVERSITY HU NG HOM, Wiley Online Library on [02/10/2025]. See the Terms and Conditions

: (https://onlinelibrary.wiley.com/terms-and-conditions) on Wiley Online Library for rules of use; OA articles are governed by the applicable Creative Commons License

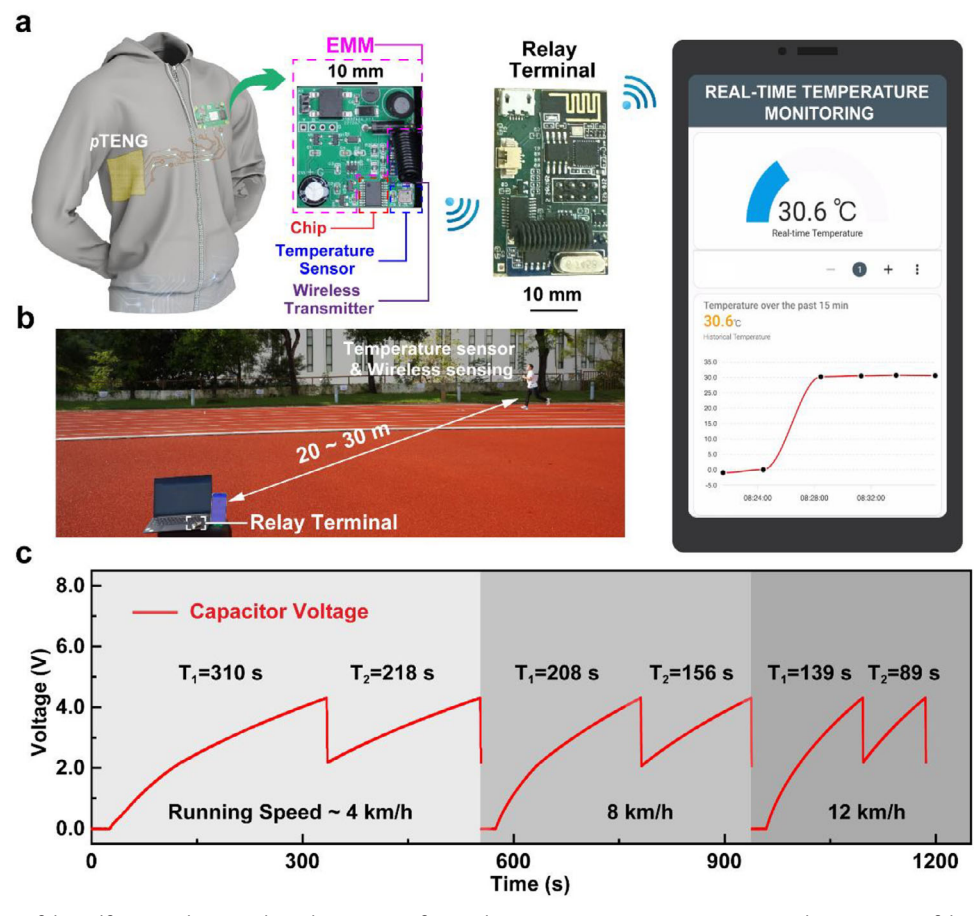


**Figure 4.** Application of the self-powered system based on pTENG for wireless temperature monitoring. a) Working process of the self-powered system based on pTENG for wireless temperature monitoring. b) Demonstration of wireless temperature monitoring during running. c) Voltage changes of the energy storage module in EMM at different running speeds ( $T_n$ : time required to charge the energy storage module in EMM to the predetermined voltage (i.e., 4.4 V, n is the number of charges).

power of 2.8 mW and an average power of 229  $\mu$ W under a 60 M $\Omega$  external load (Figure 3d). This voltage output performance can be well retained over 15000 operational cycles (Figure 3e), which is especially advantageous for long-term energy harvesting applications.

However, the pulsed AC output voltage of the pTENG cannot directly power wireless electronic devices that typically require a stable and continuous voltage supply. Though several electronic switch (E-switch) strategies have been developed for wearable TENG devices, most of them rely solely on rectifier bridges to manage the pulsed output of TENGs (Table S2, Supporting Information). [60-64] These approaches, however, are inadequate for maximizing energy harvesting, since rectifier bridges cannot dynamically match the high output impedance of the TENG, leading to inefficient charge transfer. Furthermore, these approaches generally lack effective regulation or control over the harvested energy, resulting in uncontrolled voltage rise and significant energy leakage through the load circuit. To solve this challenge, an Energy Management Module (EMM) is specifically designed for pTENG as a unified E-switch, which consists of a management unit, a storage unit, and a regulator unit (Figure 3f). The management unit, comprising of a rectifier bridge, a capacitor (C), a thyristor (SCR), a diode (D), an inductor (L), and a parallel freewheeling diode (D<sub>1</sub>), is used to regulate the voltage and impedance of the pTENG. The physical layout for the management unit is illustrated in Figure S7 (Supporting Information). When the output voltage of the pTENG, upon passing through the rectifier bridge, exceeds the reverse breakdown voltage of the diode D (i.e., 200 V in this design), SCR remains turned on (Figure S11a-i, iii, Supporting Information). At this stage, the energy generated by the pTENG accumulates in inductor L as the human body continues mechanical motion and diode D<sub>1</sub> remains closed. When the output voltage of the pTENG, upon passing through the rectifier bridge, is below the reverse breakdown voltage of the diode D, SCR remains turned off (Figure S11a-ii, iv, Supporting Information). The electrical energy generated by the pTENG is then released from inductor L to the storage unit (i.e., capacitor C<sub>1</sub>), while diode D<sub>1</sub> remains open, forming an energy conversion loop. The pTENG continuously harvests mechanical energy from human motion, leading to the SCR repeatedly switching on and off, and subsequently converting the harvested energy into electrical energy with a maximum efficiency of 50%. The converted energy is then stored in the storage unit (C<sub>1</sub>), thereby increasing the voltage of C<sub>1</sub>. To further address the need for stable DC power in electronics, we incorporate a voltage regulator unit that consists of a switch S2 and





regulator D<sub>2</sub> into EMM, which can regulate the electrical energy from capacitor C<sub>1</sub> into a stable DC electricity. Briefly, Switch S<sub>2</sub> comprises a series of monitor chips  $(Q_1 - Q_4)$ , resistors  $(R_1$  and  $R_2$ ), Zener Diode ( $D_3$ ), and capacitors ( $C_2 - C_6$ ), as well as a triode (Tr<sub>1</sub>). The detailed circuit design and physical layout for the voltage regulator unit are illustrated in Figure S12 (Supporting Information). When the voltage of capacitor C<sub>1</sub> reaches the threshold of 4.4 V (i.e., predetermined voltage value sufficient to power the wireless wearable devices demonstrated in this work), switch S<sub>2</sub> activates, achieving 2.5 V of DC electricity (Figure S13, Supporting Information). The energy released by capacitor C<sub>1</sub> during the discharge phase can be calculated using the equation  $J = \frac{1}{2} C_1 (V_{initial}^2 - V_{final}^2)$ , where J is the energy released by capacitor  $C_1$ ,  $C_1$  is the capacitance of  $C_1$  (i.e., 0.68 mF),  $V_{initial}$  is the threshold voltage that triggers the activation of switch  $\mathbf{S}_2$  (i.e., 4.4 V), and  $V_{final}$  denotes the discharge-end voltage of the storage capacitor when switch S2 is deactivated (i.e., 2.5 V), yielding ≈4.457 mJ. Such a voltage value and the amount of energy generation are sufficient to fully power a wireless sensing system, such as the temperature sensing and signal transmission demonstrated in our proof-of-concept system described in below section, which requires only 4.45 mJ for one complete sensing and transmission cycle. Compared with the conventional rectifier-only designs, this unified EMM design can significantly enhance the energy management efficiency and maintain a stable 2.5 V output for pTENG. While pTENG managed only by a rectifier bridge, which is a commonly adopted practice for regulating the output of TENG, can only charge capacitor C<sub>1</sub> (0.68 mF) to 0.29 V in 300 s, pTENG with EMM can efficiently charge C<sub>1</sub> to 3.1 V within the same time frame (Figure 3g). This comparison demonstrates a ten-fold increase in efficiency by using the developed EMM, clearly demonstrating its advantages for wearable TENG applications.

#### 2.4. pTENG for Self-Powered Wireless Temperature Monitoring

The permeable and all-textile-based pTENG, showcasing exceptionally high power output, can seamlessly integrate into a wearable format. This integration, when coupled with EMM, allows for the effective harvesting of human motion energy and the efficient conversion into electric energy for self-charging wearable electronics. As proof of concept, we develop a self-powered garment integrating the LMPT-based pTENG with EMM, the temperature sensing system, and wireless transmission. This selfpowered system operates by solely relying on the biomechanical energy converted by the pTENG, without the need for any external power supply. The pTENG is encapsulated with a layer of thermoplastic polyurethane (TPU) fiber mat for waterproof and protection purpose, and then fixed on the lateral sides of the T-shirt. Notably, the TPU-encapsulated pTENG still maintains a high moisture permeability of 600 g m<sup>-2</sup> day<sup>-1</sup> (Figure S14, Supporting Information), meeting the requirement for insensible perspiration and thermoregulation of human skin (300-600 g m<sup>-2</sup> day<sup>-1</sup>). [65,66] The pTENG is subsequently linked to EMM to create an energy-harvesting module circuit. This circuit can supply electricity to the wireless temperature sensing system that consists of a temperature sensor, a chip for processing the collected temperature data, and a wireless transmitter for transmitting the data to the relay terminal (**Figure 4a**). The relay terminal is an independent external circuit, separate from both the wireless temperature sensing system and its energy supply circuit (i.e., pTENG and its linked EMM). It consists of a chip, a wireless receiver, and a Wi-Fi module, which is powered by a battery. This setup enables the relay terminal to upload the received temperature information to the cloud through Wi-Fi technology. Afterward, the information is received and real-time displayed on a monitoring terminal (i.e., smartphone in this demonstration), through which a self-powered wireless temperature monitoring system for exercise is constructed. Detailed fabrication procedures as well as the parameters of each module in the system are described in the experimental section and summarized in Figures S15 and S16, and Tables S3–S5 (Supporting Information).

When worn by the runner, this self-powered T-shirt utilizes the integrated pTENG to harness the kinetic energy during running. The natural swinging motion of the arm during walking or running periodically compresses and releases the device, resulting in repeated contact and separation between the two triboelectric layers. This vertical mechanical deformation enables the pTENG to generate continuous electrical output under the contact-separation working mode without the need for intentional external force. The harnessed energy is then converted into electrical energy and stored in the storage module of EMM, subsequently supplying the required electricity to the wireless sensing integrated system. Upon reaching the voltage threshold of the energy storage module in EMM (i.e., 4.4 V, the predetermined voltage value sufficient to power the temperature sensing and wireless transmission (power consumption: ≈22.5 mW), the voltage is automatically regulated to a stable 2.5 V by the voltage regulator unit of EMM, which is suitable to power the wireless sensing system. Notably, the energy harvested by pTENG is sufficient to allow for the wireless and real-time transmission of the collected temperature data to the relay terminal within a distance of 20–30 m (Figure 4b; and Video \$1, Supporting Information). Once the system's electrical energy is depleted for the temperature sensing and wireless transmission, it can be replenished by continuing collecting the energy from running to reach the predetermined voltage again. This re-energizing process enables self-powered and continuous temperature monitoring during the exercise. We investigate the relationship between charging efficiency and running speed by performing treadmill-based tests. The output voltage of the pTENG at different running speeds ranging from 4 to 12 km h<sup>-1</sup> (Figure S17, Supporting Information) remains stable at ≈600 V across all tested speeds, indicating that the pTENG can reliably generate high-voltage output regardless of motion intensity. While the output voltage is independent of the running speed, the power supply capability of the pTENG is closely related to the efficiency of the energy harvesting from the human motion. Specifically, the faster the running speed, the greater the mechanical energy generated, leading to higher efficiency in energy harvesting by the pTENG. Consequently, when the running speed increases from 4 to 12 km h<sup>-1</sup>, the time required to charge the energy storage module in the EMM to 4.4 V is reduced by ≈55%, demonstrating the enhanced charging performance under faster motion. Importantly, during walking and running, occasional movements, such as jumping, arm waving, or even resting, do not affect the storage of harvested energy. The



SMQ

www.small-journal.com

output voltage will continue to increase with ongoing walking for running motions until the required voltage threshold is reached to activate the sensor operation (Figure S18, Supporting Information), allowing for the reliable operation of the temperature sensor. After consuming the power for signal transmission, running at the speed of 12 km  $h^{-1}$  can complete the energy replenishment within 89s, which is 43% faster than running at the speed of 8 km  $h^{-1}$  and 60% faster compared to running at the speed of 4 km  $h^{-1}$  (Figure 4c).

#### 3. Conclusion

In conclusion, we have introduced a permeable triboelectric nanogenerator (pTENG) with a remarkable energy output exceeding 35 V cm<sup>-2</sup>, ensuring the ability to power a wireless sensing system without hindering skin perspiration. Such high output of this pTENG is attributed to the efficient composite dielectric fibrous network formed by uniformly distributed LM nanoparticles in the electrospun LMPT, which significantly enhances the dielectric constant of the triboelectric electrode. Incorporated by a tailor-designed energy management module, pTENG can achieve a charging speed 10 times faster compared to the counterpart with commonly adopted rectifier. As a proof of concept, a smart garment integrated with a self-powered wireless temperature sensing system is constructed, which is comprised of the newly developed LMPT-based pTENG, the energy management module, the temperature sensor, and the wireless transmitter. By continuing harvesting human motion energy by the pTENG during the exercise, such a self-powered system enables the real-time tracking and display of the temperature. This integration, by incorporating high-output energy harvester, energy management module, and active wireless sensing technologies, not only reduces the reliance on external power source but also promotes the real-time and wireless health monitoring, showcasing the high application promise in body area networks for enhanced personalized healthcare and well-being monitoring.

#### 4. Experimental Section

Fabrication of LMPT: All chemicals were employed in the experiments without undergoing additional purification. The LMPT is prepared via electrospinning of an electrospinning dope mixed with the suspension of LM nanoparticles and the PVDF-TrFE solution. The suspension of LM nanoparticles was formed by probe sonication (TL-250Y, Jiangsu Tenlin Instrument Co., Ltd., China) of bulk LM in a solvent. Briefly, bulk LM (Ga: In (weight ratio: 15.1:4.9), 16 °C, Dingguan Metal Co., Ltd., China) with different masses (0.0400, 0.0800, 0.1608, 0.4082, and 0.8380 g) were added to 4 g solvent mixture of DMF (N, N-Dimethylformamide, 99.5%, DUK-SAN) and acetone (99.8%, RCI Labscan Limited) (weight ratio: 3:1) in a 20 mL glass container. The container was then placed in an ice bath, where the temperature was maintained at 0-3 °C during the probe sonication process. The probe sonication is conducted at 80% power under a burst mode (on/off, 2 s) for 2 h. The PVDF-solution was prepared by dissolving PVDF-TrFE pellets (Xinsuyuan Plastic Technology Co., Ltd., China) into the solvent mixture of DMF and acetone at a concentration of 13.66% wt. by magnetic stirring for 2 h at 75 °C. To prepare the electrospinning dope containing LM and PVDF-TrFE, the LM suspension and PVDF-TrFE solution were mixed at weight ratios of (0.339, 0.342, 0.349, 0.370, and 0.406):1 (Figure S1, Supporting Information). LMPT composite fiber mat was then fabricated by the electrospinning of the dope containing LM and PVDF-TrFE at a voltage of 14 kV (TL-Pro, Shenzhen Tongli Micro-Nano Technology Co., Ltd., China). The collection distance and a flow rate of the dope were set as 15 cm and 2.5 mL  $h^{-1},$  respectively. The humidity and temperature inside the electrospinning chamber are maintained at 55  $\pm$  5% and 35  $\pm$  5 °C, respectively. The electrospun fiber mat was collected on the Ni fabric and subsequently dried at 80 °C overnight. For comparison, PVDF-TrFE fiber mat without the incorporation of LM was fabricated with the same electrospinning conditions.

Assembly of pTENG: pTENG was assembled by stacking two pieces of triboelectric electrode fabrics, including one electrospun LMPT fiber mat on the Ni fabric as the bottom electrode (negative triboelectric layer) and one Ni fabric as the top electrode (positive triboelectric layer). To enhance the waterproof and stability of the triboelectric electrodes, a layer of TPU fiber mat was respectively electrospun on the outer sides of the LMPT electrode and Ni fabric electrode before the assembly. Finally, the obtained electrospun films were subsequently dried at 80 °C overnight. After then, these two TPU-encapsulated electrodes were connected using an elastic Kapton film to form a contact-separation structured pTENG.

Materials Characterization and Electric Measurement: The morphologies the electrospun fiber mats were investigated by Field Emission Scanning Electron Microscope (SEM, Tescan MAIA3) and Field Emission Transmission Electron Microscope (TEM, JEOL JME-2100F). The elemental characterization for the fiber mat was carried out by the energy dispersive spectroscopy in SEM. The tensile stress-strain curves of the electrospun films were obtained using an Instron 5599 universal testing system. The moisture permeability test of the samples was conducted using the cup method in accordance with the textile standard E96/E96M-13. The moisture vapor transmission rate (g/m²/day) was determined by measuring the weight loss of water vapor from a cup, which was securely covered with the test sample (test duration: 72 h). The air permeability test was conducted using an MO21S air permeability tester (SDL Americ, Inc.) in accordance with the ASTM D737-08 standard. The thickness of the electrospun films was regulated mostly by electrospinning time and characterized by high-precision thickness gauge (SYA221176471). To evaluate washing durability, a standardized washing test was carried out following the Standard AATCC 135 (Delicate program), in which the pTENG samples were placed in a washing bag and washed with a 1.8 kg fabric load for 45 min. This condition was designed to simulate practical laundering scenarios and examine the stability of the pTENG's output performance after washing.

The open-circuit voltage and charge of the pTENG were measured using a programmable electrometer (Keithley 6517B) connected with a highvoltage probe (HVP-40). The surface potential of the pTENG was characterized by using an electrostatic voltmeter (Trek 347). The LMPT sample was mounted on a motorized three-axis stage. By changing the position of the sample beneath the probe, the local surface potentials were recorded at multiple positions, and the average value along with the standard deviation was calculated to evaluate the overall surface potential distribution. The cycling stability test of the pTENG was conducted using a fatigue testing machine (LT-1, Dongguan Huaguo Precision Instrument Co., Ltd., China). The force applied to the pTENG was measured using a spoke-type load cell (JLBU-1). The capacitance of pTENG and LMPT was measured using an LCR meter (Keysight, E4980A). The relative permittivity ( $\epsilon_r$ ) of the LMPT is determined using the equation  $\epsilon_r = t_{LMPT} \cdot C_{LMPT} / S_{LMPT} / \epsilon_0$ , where  $t_{LMPT}$  is the thickness of LMPT,  $C_{LMPT}$  is capacitance of LMPT,  $S_{LMPT}$ is the measure area of LMPT, and  $\epsilon_0$  (8.854  $\times$  10<sup>-12</sup> F/m) is the vacuum dielectric constant.

Fabrication of Energy Management Module and the System Integration: The energy management module first uses a rectifier bridge, a ceramic capacitor, a thyristor, a diode, an inductor, and a parallel freewheeling diode as a management unit to regulate the voltage and impedance of the pTENG. Then, a storage capacitor was used to store the energy generated by the pTENG. Finally, switch  $S_2$ , comprising a series of monitor chips  $(Q_1 \_ Q_4)$ , Zener Diode  $(D_3)$ , resistors  $(R_1$  and  $R_2)$ , capacitors  $(C_2 \_ C_6)$ , and a triode  $(Tr_1)$ , were employed to regulate the electrical energy from the storage capacitor  $(C_1)$ , ensuring a stable DC output. The working current of  $S_2$  is  $\approx 4~\mu A$  at a maximum working voltage of 4.4 V and its operating duration is  $\approx 0.17$  s (Figure S19, Supporting Information). As such, the maximum energy consumption of  $S_2$  is  $\approx 2.992~\mu J$ , corresponding to a

www.small-journal.com

power consumption of  $\approx\!17.6~\mu\text{W}.$  This extremely low energy requirement ensures that majority of the harvested energy stored in the capacitor C<sub>1</sub> could be effectively utilized by the wireless sensing components with minimal loss during S2 operation, demonstrating the high energy efficiency of the system design and the feasibility of self-powered operation. Table S3 (Supporting Information) provides a detailed summary of the component parameters of the energy management module.

The wireless sensing integrated system primarily consists of an energy management module as the stable DC power supply, a temperature sensor, a chip, and a wireless transmitter. The chip for temperature signal processing was programmed by the software Keil. This system enables the acquisition and wireless transmission of temperature signals, consuming ≈4.45 mJ of energy (≈22.5 mW power) during the process. Figure S11 (Supporting Information) presents the detailed circuit design diagram, while Table S3 (Supporting Information) provides a comprehensive summary of the component parameters in the wireless sensing integrated sys-

The relay terminal module mainly consists of a wireless receiver, a chip, a voltage stabilizer, a lithium-ion battery, and a Wireless Fidelity (Wi-Fi) module, which could receive data from the wireless transmitter, upload it to the cloud server, and display the data in the real-time monitoring terminal (i.e., smartphones and computers in this work). The chip for temperature signal processing was programmed by the software Keil. A 400 mAh lithium-ion battery, with a nominal voltage of 3.7 V, could directly power the entire relay terminal module. Figure \$16 (Supporting Information) presents the detailed circuit design diagram, while Table S5 (Supporting Information) provides a comprehensive summary of the component parameters in the relay terminal module.

Statistical Analysis: The output data of the pTENG were directly collected from the electrometer (Keithley 6517B) without the need for further transformation or normalization. Data were presented as mean  $\pm$ standard deviation, typically based on five independent measurements. All electrical output parameters, including open-circuit voltage, short-circuit current, and transferred charge, were measured at least three times under identical conditions. All data processing was performed using Origin and Microsoft Excel.

## **Supporting Information**

Supporting Information is available from the Wiley Online Library or from the author.

# Acknowledgements

The authors acknowledge Early Career Scheme of Hong Kong (25208523), NSFC's Young Scientists Fund (52203318), General Research Fund of Hong Kong (15212021), Shenzhen Science and Technology Innovation Committee (SGDX20210823103403033), and The Hong Kong Polytechnic University (1-W28U) for the financial support. The authors thank the technical support from University Research Facility in Materials Characterization and Device Fabrication (UMF). The authors also thank Dr. Guoxu Liu from the Beijing Institute of Nanoenergy and Nanosystems, Chinese Academy of Sciences, for his assistance in the surface potential measurements of LMPT.

#### **Conflict of Interest**

The authors declare no conflict of interest.

#### **Author Contributions**

Y.Q. performed conceptualization, data curation, formal analysis, investigation, methodology, software, validation, visualization, wrote the original

draft, wrote, reviewed, and edited the draft, and provided resources. J.J. performed methodology and software. F.C. and J.Z. performed data curation. J.L. performed investigation. J.F. and Y.Y. performed formal analysis. Y.D. performed methodology. Z.Z. provided resources. Q.H. performed project administration and supervision.

# **Data Availability Statement**

The data that support the findings of this study are available in the supplementary material of this article.

## Keywords

electrospinning, liquid metal, permeable triboelectric fiber mat, selfpowered system, wireless temperature monitoring

> Received: April 13, 2025 Revised: June 22, 2025 Published online: July 3, 2025

- [1] S. Kondo, M. Kameyama, K. Imaoka, Y. Shimoi, F. Mathevet, T. Fujihara, H. Goto, H. Nakanotani, M. Yahiro, C. Adachi, Nat. Commun. 2024, 15, 8115.
- [2] J. Lord, A. Thomas, N. Treat, M. Forkin, R. Bain, P. Dulac, C. H. Behroozi, T. Mamutov, J. Fongheiser, N. Kobilansky, S. Washburn, C. Truesdell, C. Lee, P. H. Schmaelzle, Nature 2021, 598, 611.
- [3] R. A. Shveda, A. Rajappan, T. F. Yap, Z. Liu, M. D. Bell, B. Jumet, V. Sanchez, D. J. Preston, Sci. Adv. 2022, 8, abo2418.
- [4] L. Wang, Z. Fei, Y. Qi, C. Zhang, L. Zhao, Z. Jiang, R. Maeda, ACS Appl. Energy Mater. 2022, 5, 7091.
- [5] X. Han, J. Tao, Y. Liang, F. Guo, Z. Xu, W. Wu, J. Tong, M. Chen, C. Pan, J. Hao, Nat. Commun. 2024, 15, 10430.
- [6] K. Aouali, N. Kacem, N. Bouhaddi, M. Haddar, Actuators 2021, 10,
- [7] T. Wang, Energy Conv. Manag. 2023, 276, 116469.
- [8] Z. Zhou, H. Wu, J. Fu, G. Zhang, P. Li, Y. Xia, X. Wang, Y. Li, J. Yang, Nano Lett. 2024, 24, 14781.
- Y. Kuang, Z. J. Chew, J. Dunville, J. Sibson, M. Zhu, Energy Conv. Manag. 2021, 237, 114129.
- [10] L. Peng, Y. Qi, J. Liu, Y. Sun, H. Zu, X. Ru, IEEE Access 2022, 10, 111974.
- [11] M. Safaei, H. A. Sodano, S. R. Anton, Smart Mater. Struct. 2019, 28,
- [12] Z. Xu, X. Han, W. Wu, F. Li, R. Wang, H. Lu, Q. Lu, B. Ge, N. Cheng, X. Li, G. Yao, H. Hong, K. Liu, C. Pan, Light:-Sci. Appl. 2023, 12, 67.
- [13] D. Yamane, K. Tamura, K. Nota, R. Iwakawa, C.-Y. Lo, K. Miwa, S. Ono, Sens. Mater. 2022, 34, 1869.
- [14] J. Oxaal, D. Foster, M. Hella, D.-A. Borca-Tasciuc, J. Micromech. Microeng. 2015, 25, 105010.
- [15] J. Zhao, G. Zhen, G. Liu, T. Bu, W. Liu, X. Fu, P. Zhang, C. Zhang, Z. L. Wang, Nano Energy 2019, 61, 111.
- [16] Y. Zi, H. Guo, Z. Wen, M.-H. Yeh, C. Hu, Z. L. Wang, ACS Nano 2016, 10, 4797.
- [17] F.-R. Fan, Z.-Q. Tian, Z. L. Wang, Nano Energy 2012, 1, 328.
- [18] X. Fu, S. Xu, Y. Gao, X. Zhang, G. Liu, H. Zhou, Y. Lv, C. Zhang, Z. L. Wang, ACS Energy Lett. 2021, 6, 2343.
- [19] S. Wang, L. Lin, Z. L. Wang, Nano Lett. 2012, 12, 6339.
- [20] Z. L. Wang, A. C. Wang, Today 2019, 30, 34.
- [21] Y. Qi, G. Liu, T. Bu, J. Zeng, Z. Zhang, C. Zhang, Small 2022, 18,
- [22] H. Yang, Y. Pang, T. Bu, W. Liu, J. Luo, D. Jiang, C. Zhang, Z. L. Wang, Nat. Commun. 2019, 10, 2309.



- [44] Y. Hao, Y. Zhang, A. Mensah, S. Liao, P. Lv, Q. Wei, Nano Energy 2023,
- T. Zhao, S. Wang, S. Nie, Nat. Commun. 2025, 16, 383. [24] J. Wang, Y. Liu, Z. Wei, T. Liu, Y. Li, B. He, B. Luo, C. Cai, S. Zhang, M. Chi, C. Shi, S. Wang, S. Nie, Adv. Funct. Mater. 2025, 35, 2424185.
- [25] Y. Qi, J. Zhao, J. Zeng, X. Cao, Y. Qin, J. Cao, L. Gong, X. Huang, Z. Wang, G. Liu, C. Zhang, ACS Appl. Mater. Interfaces 2023, 15, 40569.

[23] Y. Liu, J. Wang, T. Liu, Z. Wei, B. Luo, M. Chi, S. Zhang, C. Cai, C. Gao,

- [26] Z. Zhou, Y. Jin, J. Fu, S. Si, M. Liu, Y. Hu, J. Gan, Y. Deng, R. Li, J. Yang, npj Flex. Electron. 2025, 9, 15.
- [27] H. Wang, L. Xu, Y. Bai, Z. L. Wang, Nat. Commun. 2020, 11, 4203.
- [28] T. Huang, X. Hao, M. Li, B. He, W. Sun, K. Zhang, L. Liao, Y. Pan, J. Huang, A. Qin, ACS Appl. Mater. Interfaces 2022, 14, 54716.
- [29] S. Chang, J. Chen, F. Liu, J. Chen, C. Zhang, H. Ni, W. Xuan, H. Jin, S. Dong, H. Guo, J. Luo, Nano Energy 2024, 131, 110271.
- [30] S. Chang, F. Liu, J. Chen, L. Xia, H. Zhou, J. Jiang, K. Dong, C. Zhang, Y. Wu, J. Chen, W. Xuan, L. Sun, H. Jin, S. Dong, J. Luo, Sci. China-Technol. Sci. 2024, 67, 949.
- [31] J. Lu, L. Xu, D. Hazarika, C. Zhang, J. Li, J. Wu, K. Zhang, R. Wan, X. Xu, J. Chen, H. Jin, S. Dong, Y. Huang, Q. Zhang, Y. Wu, J. Luo, Nano Energy 2024, 129, 110022.
- [32] L. Xia, H. Zhou, J. Chen, F. Liu, S. Chang, Y. Huang, J. Jiang, K. Dong, Y. Wu, C. Zhang, W. Xuan, S. Dong, J. Luo, Adv. Electron. Mater. 2024,
- [33] H. Zou, Y. Zhang, L. Guo, P. Wang, X. He, G. Dai, H. Zheng, C. Chen, A. C. Wang, C. Xu, Z. L. Wang, Nat. Commun. 2019, 10, 1427.
- [34] Z. Ma, Q. Huang, Q. Xu, Q. Zhuang, X. Zhao, Y. Yang, H. Qiu, Z. Yang, C. Wang, Y. Chai, Z. Zheng, Nat. Mater. 2021, 20, 859.
- [35] K. Dong, X. Peng, Z. L. Wang, Adv. Mater. 2020, 32, 1902549.
- [36] Y. Qin, X. Fu, Y. Lin, Z. Wang, J. Cao, C. Zhang, Nano Res. 2023, 16,
- [37] W. Harmon, D. Bamgboje, H. Guo, T. Hu, Z. L. Wang, Nano Energy 2020, 71, 104642,
- [38] F. Xi, Y. Pang, W. Li, T. Jiang, L. Zhang, T. Guo, G. Liu, C. Zhang, Z. L. Wang, Nano Energy 2017, 37, 168.
- [39] S. Zheng, X. Wang, W. Li, Z. Liu, Q. Li, F. Yan, Nat. Electron. 2024, 7, 576.
- [40] Y. Liu, X. Ji, J. Liang, Electron 2021, 5, 11.
- [41] H. Kim, J. Lee, U. Heo, D. K. Jayashankar, K.-C. Agno, Y. Kim, C. Y. Kim, Y. Oh, S.-H. Byun, B. Choi, H. Jeong, W.-H. Yeo, Z. Li, S. Park, J. Xiao, J. Kim, J.-W. Jeong, Sci. Adv. 2024, 10, adk5260.
- [42] Q. Ye, Y. Wu, Y. Qi, L. Shi, S. Huang, L. Zhang, M. Li, W. Li, X. Zeng, H. Wo, X. Wang, S. Dong, S. Ramakrishna, J. Luo, Nano Energy 2019,
- [43] S. Chen, Y. Zhang, Y. Li, P. Wang, ACS Appl. Polym. Mater. 2024, 6,

- 109, 108291.
- [45] P. Jia, L. Wang, X. Yao, D. Zhang, H. Lin, Y. Li, Y. Chen, J. Xiong, Macromol. Mater. Eng. 2022, 307, 2200128.
- [46] F. Jiang, X. Zhou, J. Lv, J. Chen, J. Chen, H. Kongcharoen, Y. Zhang, P. S. Lee, Adv. Mater. 2022, 34, 2200042.
- [47] T. D. Khanh, J. S. Meena, S. B. Choi, J.-W. Kim, Mater. Today Adv. 2023, 20, 100427.
- [48] Y. Li, S. Xiao, X. Zhang, P. Jia, S. Tian, C. Pan, F. Zeng, D. Chen, Y. Chen, J. Tang, J. Xiong, Nano Energy 2022, 98, 107347.
- [49] Y. Li, J. Xiong, J. Lv, J. Chen, D. Gao, X. Zhang, P. S. Lee, Nano Energy 2020, 78, 105358.
- [50] Z. Li, M. Zhu, J. Shen, Q. Qiu, J. Yu, B. Ding, Adv. Funct. Mater. 2020, 30. 1908411.
- [51] H.-J. Qiu, W.-Z. Song, X.-X. Wang, J. Zhang, Z. Fan, M. Yu, S. Ramakrishna, Y.-Z. Long, Nano Energy 2019, 58, 536.
- [52] H. Wang, H. Sakamoto, H. Asai, J.-H. Zhang, T. Meboso, Y. Uchiyama, E. Kobayashi, E. Takamura, S.-I. Suye, Nano Energy 2021, 90, 106515.
- [53] Y. Yu, H. Wu, Y. Yu, J. Yan, J. Shi, H. Morikawa, W. Lyu, C. Zhu, Chem. Eng. J. 2024, 490, 151546.
- [54] L. Zheng, M. Zhu, B. Wu, Z. Li, S. Sun, P. Wu, Sci. Adv. 2021, 7, abg4041.
- [55] J. Yang, J. Cao, J. Han, Y. Xiong, L. Luo, X. Dan, Y. Yang, L. Li, J. Sun, Q. Sun, Nano Energy 2022, 101, 107582.
- [56] H.-W. Zhou, C. Zhao, Z.-Y. Zhao, J.-C. Jiang, H.-L. Jin, S. Wang, S. Pan, M.-Y. Xu, Y.-H. Chen, H.-M. Jin, Rare Met. 2023, 43, 1186.
- [57] Y. Liu, J. Luo, K. Gao, H. Li, P. He, W. Zhao, Mater. Today Commun. **2025**. 44. 112151.
- [58] L. J. Briggs, J. Chem. Phys. 1957, 26, 784.
- [59] S. Niu, S. Wang, L. Lin, Y. Liu, Y. S. Zhou, Y. Hu, Z. L. Wang, Energy Environ. Sci. 2013, 6, 3576.
- [60] A. R. Mule, B. Dudem, H. Patnam, S. A. Graham, J. S. Yu, ACS Sustainable Chem. Eng. 2019, 7, 16450.
- [61] M. Qu, L. Shen, J. Wang, N. Zhang, Y. Pang, Y. Wu, J. Ge, L. Peng, J. Yang, J. He, ACS Appl. Nano Mater. 2022, 5, 9840.
- [62] P. Munirathinam, A. Chandrasekhar, Sustain. Mater. Technol. 2023, 37 00700
- [63] H. Patnam, S. A. Graham, P. Manchi, M. V. Paranjape, Y. S. Huh, J. S. Yu, Adv. Compos. Hybrid Mater. 2024, 7, 56.
- [64] M. U. Khan, S. M. Ansari, H. M. Aldosari, B. Mohammad, Energy Conv. Manag. 2025, 26, 100976.
- [65] Q. Huang, Z. Zheng, ACS Nano 2022, 16, 15537.
- [66] Z. Ma, Q. Huang, Q. Xu, Q. Zhuang, X. Zhao, Y. Yang, H. Qiu, Z. Yang, C. Wang, Y. Chai, Z. Zheng, Nat. Mater. 2021, 20, 859.